
Conservative Flows: A New Paradigm of Generative Models

Eshed Gal

The University of British Columbia
Vancouver, Canada
eshedg@cs.ubc.ca

Md Shahriar Rahim Siddiqui

The University of British Columbia
Vancouver, Canada
shahriar.siddiqui@ubc.ca

Moshe Eliasof

University of Cambridge
Cambridge, United Kingdom
me532@cam.ac.uk

Eldad Haber

The University of British Columbia
Vancouver, Canada
ehaber@eoas.ubc.ca

Abstract

Modern generative modeling is dominated by transport from a noise prior to data. We propose an alternative paradigm in which generation is performed by a discrete stochastic dynamics that leaves the data distribution invariant, initialized from data-supported states rather than from noise. The framework can utilize any pretrained flow model. We develop two probability-preserving sampling mechanisms, a corrected Langevin dynamics with a Metropolis adjustment and a predictor-corrector flow, that operate directly on existing checkpoints. We validate the framework on a synthetic Swiss-roll target, ImageNet-256 and Oxford Flowers-102, where our samplers consistently improve over the original generation procedures.

1 Introduction

Generative modeling has been dominated by methods that construct a transport from a simple reference law, typically, Gaussian noise, to a complex data distribution [1, 2]. In score and flow-based diffusion models [3, 4, 5] this is realized by perturbing data through a forward noising process and learning score fields for the resulting family of intermediate distributions; sampling reverses the dynamics from noise back to data [6, 7, 8, 9, 10, 11, 5].

In this paper, we propose a paradigm shift for data generation. Particularly, instead of learning a global transport from noise to data, we seek to construct a discrete stochastic dynamics

$$x_0, x_1, x_2, \dots \quad (1)$$

such that

$$x_0 \sim p, \quad x_j \sim p \quad \text{for all generation steps } j \geq 1, \quad (2)$$

where p denotes the data distribution. In other words, our approach states that rather than learning how to move *toward* the data distribution from an initial prior, we learn how to move *within* the data distribution while preserving it at every step. As such, our approach shifts the goal of generative models from *transport* to *invariance*: rather than transforming noise into data, the sampler maintains the data distribution under a learned probability-conserving dynamics. An illustration of our paradigm is illustrated in Figure 1.

This viewpoint is particularly natural in modern augmented retrieval systems [12] and latent generative pipelines [13]. In such systems, generation does not begin from an information-less state. Instead, one has access to existing valid examples, nearest neighbors, memory entries, or latent codes that

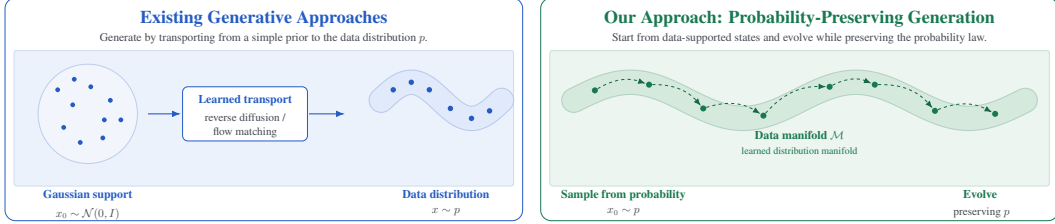


Figure 1: From transport to invariance. Existing generative models produce samples by transporting Gaussian noise to the data distribution. Our approach instead starts from data-supported states and evolves them through probability-preserving dynamics. By keeping the process on high-probability regions of the data manifold, this enables faithful sample variation, improved data fidelity, and efficient reuse of pretrained generative models.

already lie near the target distribution of interest [14]. In such settings, starting from pure noise is not the only viable option, and may not even be the most natural one. If one can start the generation process from data-supported states, then a probability-preserving dynamics becomes a compelling alternative to the common approach of noise-to-data generation.

At an infinitesimal level, Langevin dynamics, which is at the heart of modern generative models [15, 8], provides precisely this intuition [16]. That is, if $s(x) = \nabla \log p(x)$ is the score of the target density, then under standard regularity assumptions, the continuous-time diffusion, that reads:

$$dX_t = s(X_t) dt + \sqrt{2} dW_t, \quad (3)$$

preserves p as an invariant measure [17]. Thus, in continuous time, score-based dynamics already define a probability-preserving evolution. The difficulty arises *after* discretization. That is, the finite-step Langevin update defined by

$$x_{j+1} = x_j + h s(x_j) + \sqrt{2h} \xi_j, \quad \xi_j \sim \mathcal{N}(0, I), \quad (4)$$

has the correct infinitesimal behavior, but it does not preserve p exactly for finite h . This discrepancy is negligible for sufficiently small steps, but it changes the distribution, and therefore breaks the central requirement in Equation (2) [18]. Our starting point is that a generative model based on stationary dynamics, i.e., probability-preserving, as envisioned in our paradigm, should address this issue directly.

We therefore develop two probability-preserving mechanisms that start from samples already drawn from the density of interest. The *first* is a corrected Langevin dynamics based on a conservative score, or equivalently a denoiser. In its score-based form, the correction restores invariance of p ; in its denoiser-based form, it naturally acts on a Gaussian-smoothed law p_σ and therefore preserves p_σ . The *second* is a predictor–corrector flow construction: starting from $x \sim p$, one first adds a controlled amount of noise to move the sample to an intermediate bridge distribution, and then uses a learned flow or direct solution map to return it to p . Thus we present two distinct but related ways to probe a probability density when initialization already lies on, or near, that density. Notably, in both cases, the required score, denoiser, or flow, can be obtained directly from a pretrained flow-matching model, so neither mechanism requires training a new generative model from scratch.

The role of retrieval is then conceptually simple. Generation is performed by initializing the sampler from retrieved data points or retrieved latent codes, and then stepping forward with one of these probability-preserving mechanisms. In the ideal case there is no burn-in, since the chain starts from the target law itself; more generally, retrieved initializations place the sampler in a high-probability region of the relevant data manifold. This makes the framework especially attractive in latent spaces, where retrieval is natural, geometry is smoother, and local stochastic exploration can produce meaningful variation at lower computational cost [19]. We discuss related works in Appendix A.

The resulting approach differs from both standard diffusion models and classical energy-based modeling. Diffusion models learn a reverse transport from noise through a family of perturbed distributions [8, 1]. This typically requires learning a time-dependent score field $s(x, t)$ across many noise levels. In contrast, our first method does not require such a family of scores: because generation is initialized from data-supported states and proceeds by local probability-preserving moves, it is sufficient to learn a single conservative score field, or one associated with a small fixed noise level.

Energy-based models, by contrast, typically learn a scalar energy and then sample by approximate Langevin dynamics, often from noise or from a replay mechanism [20]. Our approach instead begins from data-supported states and then either uses a corrected score/denoiser-based move or a predictor–corrector flow move. **A key practical advantage** of our approach is the ability to use pretrained flow matching models. Similar to [21], our framework can be applied directly on top of such models, inheriting their manifold-aware dynamics *with no further training*. Recent work has also emphasized the importance of conservation in score-based models and explored Metropolis-type corrections based on line integration of the score [22, 23]; our contribution is to combine these ideas into a generative framework whose organizing principle is not reverse noising, but stationary probing of the data distribution itself.

We view this as a new paradigm for generative modeling. The central object is not a transport map from a simple prior, but a stochastic dynamics that preserves the relevant law. The central initialization is not Gaussian noise, but retrieved or observed data-supported states. And the central learning problem is not to model a sequence of noisy marginals, but either to learn a conservative score or denoiser together with a discrete correction, or to learn a local flow that maps partially noised samples back to the target law. In this sense, the proposed framework replaces noise-to-data generation by retrieval-seeded stationary generation. In the ideal setting of an exact conservative score and exact line integration, the first mechanism preserves the appropriate target law exactly; in the ideal setting of an exact bridge flow, the second mechanism preserves p exactly. In practice, the quality of these approximations depends on the learned score, denoiser, or flow model, and on the numerical approximation used in the correction step.

2 Method

We seek generative dynamics that leave a target law invariant. Throughout, p denotes the target data density on \mathbb{R}^d , and we assume access to samples $x \sim p$. We will use two related invariant laws. The score-based and denoiser-based Metropolis constructions operate on a Gaussian-smoothed distribution

$$p_\sigma = p * \mathcal{N}(0, \sigma^2 I),$$

and therefore leave p_σ invariant. In contrast, the predictor–corrector flow construction described later returns partially noised samples directly to the target law p , and therefore leaves p invariant in the ideal case. Keeping this distinction explicit is important for both the theory and the experiments.

2.1 On the necessity of Langevin Dynamics Correction

A natural starting point is overdamped Langevin dynamics

$$dX_t = s(X_t) dt + \sqrt{2} dW_t, \quad s(x) = \nabla \log p(x), \quad (5)$$

which preserves p in continuous time under standard regularity assumptions [17]. Thus, at the infinitesimal level, Langevin dynamics is probability-conserving.

The difficulty appears after discretization. The Euler–Maruyama step is

$$y = x + h s(x) + \sqrt{2h} z, \quad z \sim \mathcal{N}(0, I), \quad (6)$$

which is the **Unadjusted Langevin Algorithm** (ULA) [24]. Although Equation (6) has the correct local geometry, it does not preserve the target law exactly for finite step size.

A Gaussian example makes this explicit. If

$$p(x) = \mathcal{N}(0, I), \quad s(x) = -x,$$

then Equation (6) becomes

$$y = (1 - h)x + \sqrt{2h} z.$$

If $x \sim \mathcal{N}(0, I)$, then

$$y \sim \mathcal{N}(0, (1 + h^2)I),$$

which differs from p for every $h > 0$. Even in this simplest case, the discretized Langevin step is not probability-invariant.

This is the basic issue: Langevin dynamics is correct in continuous time, but its explicit discretization changes the law. The first part of our method corrects this finite-step error.

2.2 Corrected Langevin Dynamics and a Denoiser formulation

Starting from the proposal, Equation (6), define the deterministic part of the update by

$$D_h(x) := x + h s_\theta(x), \quad (7)$$

so that the proposal can be written as

$$y = D_h(x) + \sqrt{2h} z, \quad z \sim \mathcal{N}(0, I), \quad (8)$$

with proposal density

$$q_h(y | x) = \mathcal{N}(y; D_h(x), 2h I). \quad (9)$$

When p is known up to a normalizing constant, the standard correction is **Metropolis-Adjusted Langevin Algorithm (MALA)** [17, 25]. Its Metropolis–Hastings log-ratio is

$$\log r(x, y) = \log p(y) - \log p(x) + \log q_h(x | y) - \log q_h(y | x), \quad (10)$$

and the proposal is accepted with probability

$$\alpha(x, y) = \min\{1, \exp(\log r(x, y))\}. \quad (11)$$

This correction restores invariance of p .

In generative modeling, however, p is not available explicitly. To resolve this problem, we assume access to a learned score field s_θ . If this field is conservative, then the missing log-density difference can be recovered by line integration:

$$\Delta_{D_h}(x, y) := \frac{1}{h} \int_0^1 \left\langle D_h(x + t(y-x)) - (x + t(y-x)), y-x \right\rangle dt. \quad (12)$$

The corrected acceptance ratio is therefore

$$\log r_{D_h}(x, y) = \Delta_{D_h}(x, y) + \log q_h(x | y) - \log q_h(y | x), \quad (13)$$

and the proposal is accepted with probability

$$\alpha_{D_h}(x, y) = \min\{1, \exp(\log r_{D_h}(x, y))\}. \quad (14)$$

When $D_h(x) = x + h \nabla \log p(x)$ and the integral Equation (12) is evaluated exactly, this reduces to dMALA and preserves p .

This notation becomes especially useful when D_h is obtained from a denoiser. Let p_σ be the Gaussian-smoothed density, and let D_σ be a denoiser trained to predict the clean sample from a noisy observation. Tweedie’s identity gives

$$D_\sigma(y) = y + \sigma^2 \nabla \log p_\sigma(y). \quad (15)$$

Thus D_σ is exactly of the form Equation (7) with $h = \sigma^2$ and $s_\sigma(y) = \nabla \log p_\sigma(y)$. The proposal becomes

$$y = D_\sigma(x) + \sqrt{2} \sigma z, \quad z \sim \mathcal{N}(0, I), \quad (16)$$

with proposal density

$$q_\sigma(y | x) = \mathcal{N}(y; D_\sigma(x), 2\sigma^2 I). \quad (17)$$

The corresponding line integral is

$$\Delta_{D_\sigma}(x, y) = \frac{1}{\sigma^2} \int_0^1 \left\langle D_\sigma(x + t(y-x)) - (x + t(y-x)), y-x \right\rangle dt, \quad (18)$$

so the exact correction leaves the smoothed density p_σ invariant. This point is important: the denoiser-based Metropolis construction preserves p_σ , not the original target law p .

A further simplification is obtained by approximating Equation (18) with the trapezoidal rule. Define the residual

$$r_\sigma(x) := D_\sigma(x) - x. \quad (19)$$

Then,

$$\Delta_{D_\sigma}(x, y) \approx \frac{1}{2\sigma^2} \langle r_\sigma(x) + r_\sigma(y), y-x \rangle. \quad (20)$$

Combining this with the Gaussian proposal ratio, the cross terms cancel and the approximate log-acceptance ratio becomes

$$\log r_{D_\sigma}(x, y) \approx \frac{1}{4\sigma^2} \left(\|D_\sigma(x) - x\|^2 - \|D_\sigma(y) - y\|^2 \right). \quad (21)$$

This yields a particularly simple denoiser-based sampler requiring only two evaluations of D_σ per step. We refer to this sampler as **denoising MALA**, or **dMALA**, in short, because it reduces to the standard Metropolis-adjusted Langevin algorithm in the conservative-score, exact-line-integration limit.

Training the denoiser is straightforward. For σ fixed or sampled from a small interval close to 0, one minimizes

$$\mathcal{L}_{\text{denoise}} = \mathbb{E}_{x, \varepsilon, \sigma} \|D_\sigma(x + \sigma\varepsilon) - x\|^2, \quad \varepsilon \sim \mathcal{N}(0, I). \quad (22)$$

In order to encourage a conservative score field, we use the classical fact from vector calculus [26] that if $s : \Omega \subset \mathbb{R}^d \rightarrow \mathbb{R}^d$ is C^1 , Ω is simply connected, and its Jacobian $\nabla s(x)$ is symmetric for every $x \in \Omega$, then s is a gradient field; that is, there exists a scalar potential ϕ such that

$$s(x) = \nabla\phi(x).$$

Since

$$J_{D_\sigma}(x) = I + \sigma^2 J_{s_\sigma}(x), \quad (23)$$

the denoiser Jacobian $J_{D_\sigma}(x)$ is symmetric if and only if the score Jacobian $J_{s_\sigma}(x)$ is symmetric. Therefore, to encourage a conservative score field, it is sufficient to regularize the denoiser Jacobian. We do so through

$$\mathcal{L}_{\text{sym}}^D(x) = \mathbb{E}_v \|J_{D_\sigma}(x)v - J_{D_\sigma}(x)^\top v\|^2, \quad (24)$$

which is numerically more stable than regularizing the score directly.

A practical reason to work with a denoiser is that strong pretrained flow-matching models are often already available. Rather than training a separate score network, one can extract a denoiser directly from the bridge on which the flow model was trained. This keeps the method internally consistent: the same interpolation used in flow training defines the denoiser used at sampling time. The corresponding construction is described in Appendix B.

Example 1 (ULA versus corrected Langevin - MALA - on a Swiss-roll-like target). *To illustrate the need for correction, we consider a two-dimensional Swiss-roll-like target density and initialize particles from the target distribution. We then evolve them using either the unadjusted Langevin algorithm (ULA) or the corrected dynamics above. Since both methods start from $x_0 \sim p$, an ideal probability-preserving process should satisfy $x_k \sim p$ for all k . In practice, ULA drifts away from the target, while the corrected dynamics remains close to the original distribution.*

2.3 A predictor–corrector approach for probability-invariant flow

The previous subsection used a local stochastic proposal together with a Metropolis correction. In the denoiser formulation, this yields a Markov chain [27] whose invariant law is the smoothed distribution p_σ . We now describe a different construction that targets the original law p directly.

The corrected Langevin dynamics above uses Langevin as a local predictor and a Metropolis step as a correctness mechanism: if the proposal is inaccurate, it is simply rejected. This is effective when the local geometry is mild, but for highly curved or irregular manifolds the predictor can be poor, leading to low acceptance rates and consequently very slow exploration. In such settings, insisting that every proposal remain close to the high-probability region at all times may be unnecessarily restrictive. The flow-based approach considered here follows a different principle. Instead of proposing a local step and rejecting it when it leaves the manifold, we first allow the sample

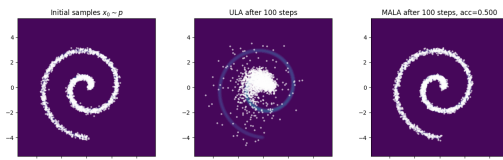


Figure 2: Comparison between unadjusted Langevin dynamics (ULA) and the corrected dynamics (dMALA) on a Swiss-roll-like distribution. ULA drifts away from the target, while the corrected dynamics preserves it.

to move a controlled distance away from the target distribution by adding a small amount of noise, and then use a learned flow to transport it back to the data distribution. This predictor–corrector mechanism can make substantial moves even when the geometry of the manifold is highly nonlinear, while still preserving the target law in the ideal case.

Let $p_1 = p$ denote the target law, let $p_0 = \mathcal{N}(0, I)$, and consider the linear bridge

$$x_t = (1 - t)z + tx, \quad x \sim p_1, \quad z \sim p_0. \quad (25)$$

We denote by p_t the law of x_t . Thus p_t interpolates between noise at $t = 0$ and data at $t = 1$.

Suppose now that we have trained a flow model associated with this bridge. This may be represented either by a velocity field

$$\dot{x} = v_\theta(x, t), \quad x(\tau) = x_\tau, \quad t \in [\tau, 1], \quad (26)$$

with flow map $\Phi_{\theta, t \rightarrow s}$, or by a direct solution map

$$f_\theta(x_t, t, s) \approx \Phi_{t \rightarrow s}(x_t). \quad (27)$$

In our experiments, the latter is particularly convenient because it avoids numerical ODE integration at sampling time.

Starting from $x \sim p_1$, choose $\tau \in (0, 1)$, typically close to 1, and draw

$$\hat{x} = (1 - \tau)z + \tau x, \quad z \sim \mathcal{N}(0, I). \quad (28)$$

Since $\hat{x} \sim p_\tau$, this predictor step moves the sample slightly away from the target distribution while remaining on the bridge. We then apply the learned flow from time τ back to time 1:

$$x^+ = \Phi_{\theta, \tau \rightarrow 1}(\hat{x}), \approx x^+ = f_\theta(\hat{x}, \tau, 1). \quad (29)$$

Under an exact flow model, this move is probability-invariant.

Proposition 1 (Probability invariance of the predictor–corrector kernel). *Assume that for every $0 \leq t \leq s \leq 1$,*

$$(\Phi_{t \rightarrow s})_\# p_t = p_s. \quad (30)$$

Let $x \sim p_1$, draw $z \sim p_0$ independently, form \hat{x} by Equation (28), and set $x^+ = \Phi_{\tau \rightarrow 1}(\hat{x})$. Then $x^+ \sim p_1 = p$.

Proof. By construction, $\hat{x} \sim p_\tau$. Applying the exact flow map from τ to 1 gives

$$x^+ = \Phi_{\tau \rightarrow 1}(\hat{x}) \sim (\Phi_{\tau \rightarrow 1})_\# p_\tau = p_1. \quad \square$$

This yields a probability-preserving Markov kernel

$$K_\tau(x, \cdot) : \quad x \mapsto x^+ = \Phi_{\theta, \tau \rightarrow 1}((1 - \tau)z + \tau x), \quad z \sim \mathcal{N}(0, I). \quad (31)$$

For τ close to 1, this is a local move. Smaller values of τ give stronger refreshment and potentially better mixing, but rely more heavily on the accuracy of the learned flow. A practical consequence is that the model only needs to be accurate near the data end of the bridge. Since the sampler uses τ close to 1, it is sufficient to train on times $t \in [\tau_{\min}, 1]$ rather than on the full interval $[0, 1]$.

Conceptually, this construction replaces Metropolis rejection by a learned return map to the target distribution. The predictor adds a controlled amount of noise, and the corrector follows the learned probability flow back to p . This provides a second route to invariance, now based on flow matching rather than corrected Langevin dynamics.

3 Experiments

We design experiments to address the following research questions: **(i)** Does the corrected dynamics preserve a target law in practice, where unadjusted Langevin discretization drifts away from it?; **(ii)** Do the two probability-preserving samplers improve over the baseline samplers of their pretrained backbones on ImageNet-256?; **(iii)** How do the two samplers compare to each other, both in long-run exploration on a known density and across operating points on a high-dimensional benchmark?; and **(iv)** How do the samplers behave under varying chain length and computational budget?

Table 1: SoFlow-denoiser MALA ablation. This method preserves the smoothed law p_σ .

t_{noise}	σ	steps	Acc. rate	NLL to p_σ	MMD to p_σ	Mean move
0.90	0.111	200	0.896	2.912	0.016	1.508
0.95	0.053	200	0.960	2.386	0.013	0.813
0.98	0.020	200	0.989	1.733	0.017	0.370

Baselines. For ImageNet-256, we compare against the official 1-NFE solution-operator sampler of SoFlow-XL/2-cond [28] and no-CFG 400-step Euler sampling using SiT-REPA-XL [29], and we operate within the latent space of the Stable Diffusion VAE [13], consistent with the pretrained baselines. For the synthetic Swiss-roll experiment, the relevant baseline is the unadjusted Langevin algorithm (ULA) [24]. All ImageNet-256 metrics are computed on 50,000 generated samples against the ADM ImageNet-256 reference batch. We present further experimental results on the Oxford-Flowers-102 dataset in Appendix E.1

3.1 Probability preservation on a synthetic target

We compare the two probability-preserving mechanisms of Section 2 on a two-dimensional Swiss-roll-like target density given by a Gaussian mixture supported along a spiral. This problem is useful since the target density is known exactly, so we can evaluate negative log-likelihood under the true law, while the geometry is sufficiently nonlinear to make long-term mixing visually and quantitatively informative. In all experiments below, both methods use the same pretrained SoFlow model [28]. dMALA is implemented through the denoiser extracted from that flow model, while the predictor-corrector method uses the direct solution map itself.

A key distinction between the two methods is the law they preserve. dMALA’s dynamics is designed to preserve the smoothed distribution p_σ , where the smoothing level is determined by the denoising time $1 - \tau = t_{\text{noise}}$. In contrast, the predictor-corrector construction targets the original distribution p directly. For this reason, the quantitative evaluation is performed against p_σ for dMALA and against p for the predictor-corrector method.

Denoiser-Metropolis (dMALA). We first evaluate the corrected Langevin dynamics of Section 2.2 using the denoiser extracted from the pretrained SoFlow model. We vary the denoising time t_{noise} , and therefore the implied smoothing level $\sigma = (1 - t_{\text{noise}})/t_{\text{noise}}$, while fixing the proposal step size to $dt = \sigma^2$. Table 1 reports the resulting acceptance rate, the negative log-likelihood with respect to p_σ , the MMD to samples drawn from p_σ , and the mean displacement after 200 steps. The behavior of the dMALA step is observed in Table 1.

Predictor-corrector flow. We next evaluate the predictor-corrector mechanism of Section 2.3. Starting from $x \sim p$, we partially noise the sample to the bridge distribution p_τ , and then use the learned SoFlow map to return it to p . Table 2 reports results for several values of τ , including the negative log-likelihood with respect to the true target law p , the MMD to samples drawn from p , and the mean displacement after 200 steps.

Comparison of the two mechanisms. Finally, Figure 3 compares the long-run trajectories of the two methods side by side using the same initial clean seeds. For the predictor-corrector method, these clean seeds are used directly. For dMALA, the same seeds are first perturbed by the

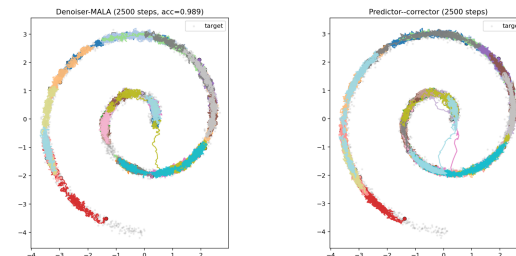


Figure 3: Side-by-side comparison. Left: dMALA trajectories on p_σ . Right: predictor-corrector flow on p . Both use 32 particles for 2500 steps. The figure demonstrates long chain behavior of both methods. Clearly, they continue to move broadly along the roll while remaining on the correct law.

Table 2: Predictor-corrector flow ablation. This method targets the original law p .

tau	steps	NLL to p	MMD to p	Mean move
0.70	200	8.994	0.057	2.811
0.85	200	3.378	0.025	1.633
0.95	200	1.760	0.020	0.568

Table 3: Predictor–corrector and dMALA flows on ImageNet-256.

Backbone	Method / setting	FID ↓	sFID ↓	IS ↑	Precision ↑	Recall ↑
<i>SoFlow-XL/2-cond backbone</i>						
	Baseline (1-NFE)	2.96	4.60	238.53	0.795	0.564
	Predictor–Corrector, $K = 10, t_{\text{noise}} = 0.3$	2.28	5.47	297.37	0.79	0.62
	dMALA, $K = 10, \sigma = 0.3$	1.70	5.05	300.04	0.79	0.65
	Predictor–Corrector, $K = 20, t_{\text{noise}} = 0.5$	4.67	5.33	349.84	0.87	0.50
	dMALA, $K = 20, \sigma = 0.3$	2.17	5.81	306.25	0.80	0.62
<i>SiT-REPA-XL backbone</i>						
	Baseline (no CFG, 400 Euler steps)	6.61	5.62	152.52	0.68	0.69
	Predictor–Corrector, $K = 10, t_{\text{noise}} = 0.3$	3.11	6.06	220.35	0.73	0.68
	dMALA, $K = 10, \sigma = 0.3$	1.93	5.62	241.20	0.74	0.70
	Predictor–Corrector, $K = 20, t_{\text{noise}} = 0.5$	3.06	6.24	199.50	0.72	0.69
	dMALA, $K = 20, \sigma = 0.3$	1.79	5.14	236.03	0.74	0.71

corresponding Gaussian smoothing noise so that the initialization is consistent with the preserved law p_σ . This comparison is intended to highlight the different exploration behavior of the two probability-preserving constructions. dMALA makes local accept/reject moves on the smoothed law, whereas the predictor–corrector method makes larger nonlocal moves by temporarily stepping away from the manifold and then returning to the target distribution through the learned flow.

Overall, the experiments are designed to illustrate the tradeoff between the two constructions. dMALA is a corrected local sampler with an explicit accept/reject mechanism and a well-defined invariant smoothed law p_σ . The predictor–corrector method, by contrast, targets the original law p directly and can make larger moves by using the learned flow as a return map to the data distribution. The Swiss-roll experiments provide a controlled setting in which both behaviors can be observed clearly.

3.2 ImageNet-256 generation

We evaluate the two proposed stationary generation mechanisms on ImageNet-256 [30] using two pre-trained latent flow backbones: SoFlow-XL/2-cond [28] and SiT-REPA-XL [29]. All metrics are computed on 50,000 generated samples against the ADM ImageNet-256 reference batch. For SoFlow, the baseline is the official 1-NFE solution-operator sampler. For SiT-REPA, the baseline is the no-CFG Euler sampler used in our implementation. Our methods initialize from data-supported VAE latents, apply a local noising step, and then return to the data distribution using either the predictor–corrector map or the dMALA correction. The results of this experiment are shown in Table 3, which clearly shows that both methods give diverse enough images (Recall and IS scores) while maintaining very low FID.

Long Chain Generation: In the next experiment we test how the methods behave for longer chains. To this end we increase K (the number of steps in the chain) and compute the same metrics. The results for dMALA and Predictor-corrector are presented in Table 4. The table shows only mild deterioration with the length of the chain. This is expected for approximate pretrained flows: although the ideal kernels are probability-preserving, score approximation error by the pretrained model can accumulate over repeated applications. Samples from this run can be observed in Figure 4 and in high resolution in Figure 5.



Figure 4: Visualization of ImageNet256 for two methods (Predictor–Corrector and dMALA) and two models (SoFlow-XL/2 and REPA SiT-XL/2). The first column shows the original image; each subsequent column shows the sample after an additional 50 iterations, up to 200 total. A high resolution version is provided in Appendix G.1.

Table 4: Long-chain behavior of dMALA and Predictor-Corrector on ImageNet-256 with SoFlow-XL/2-cond. dMALA uses denoiser noise level $\sigma = 0.3$; Predictor-Corrector uses bridge noise $t_{\text{noise}} = 0.3$; K denotes the number of iterations. Acc. rate is the running mean Metropolis acceptance probability.

Method	K	Acc. rate	FID \downarrow	sFID \downarrow	IS \uparrow	Precision \uparrow	Recall \uparrow
Baseline (1-NFE)	–	–	2.96	4.60	238.53	0.80	0.56
dMALA	50	0.76	3.23	7.72	313.29	0.81	0.57
	100	0.54	4.34	10.40	308.11	0.82	0.52
	150	0.53	5.07	12.45	301.23	0.81	0.49
	200	0.53	5.61	14.26	294.47	0.81	0.47
Pred.–Corr.	50	–	3.96	8.90	313.48	0.82	0.53
	100	–	5.18	12.14	304.34	0.81	0.48
	150	–	5.93	14.64	290.25	0.80	0.46
	200	–	6.46	16.48	278.84	0.79	0.45

Computational efficiency. Beyond chain length, the predictor–corrector mechanism is also competitive in compute. With the SiT-REPA-XL backbone, 200 model calls (number of function evaluations - NFEs) attain FID 4.91, lower than the 6.51 FID of 800-step forward-Euler integration of the same backbone (Section E.3, Table 8).

We additionally evaluate our methods on the Oxford Flowers-102 dataset [31]. The quantitative results are detailed in Section E.1, and the corresponding visualizations are provided in Section G.2.

4 Discussion and Conclusion

We have proposed a generative modeling framework in which the central operation is not transport from noise to data, but approximate invariance of the data law under a probability-preserving dynamics. Two mechanisms instantiate this principle. The first is a corrected Langevin dynamics whose Metropolis adjustment preserves a Gaussian-smoothed law p_σ . The second is a predictor–corrector flow that maps partially noised samples back toward the original law p . In the ideal-model setting, both define invariant kernels; in practice, they can be implemented using quantities available from pretrained flow-matching models, and therefore can be applied on top of public checkpoints without retraining. The broader impact of our method is discussed in Appendix F.

Limitations: The effectiveness of both the Denoiser-Metropolis (dMALA) and Predictor–Corrector mechanisms is bound by the quality of the underlying pretrained flow or score-based model. Although the ideal kernels are probability-preserving in their respective ideal-model settings, approximation to the score model can accumulate errors over repeated applications of the kernel. We explicitly characterize this behavior in Table 4. Our empirical validation is also restricted to continuous benchmarks (Swiss-roll, Oxford Flowers-102, ImageNet-256). Extending this paradigm to discrete domains such as text generation, where bridge models have only recently emerged, is left to future work.

The experiments support four main conclusions. First, the quantitative results in Tables 1 and 2 show the same behavior for the smoothed law p_σ and the original law p , respectively. Second, both samplers improve FID over the baseline sampler of every backbone tested. (Table 3). Third, the two samplers occupy different operating regimes: dMALA with small smoothing gives the lowest FID, whereas the predictor-corrector mechanism trades some FID for higher Inception Score and Precision. This is consistent with the qualitative behavior in Figure 3: dMALA performs local accept/reject moves, while predictor-corrector sampling makes larger non-local moves through the learned flow. Finally, chain length and NFE budget provide graceful trade-offs. Performance degrades smoothly on ImageNet-256, consistent with accumulated approximation errors in the pretrained backbone (Table 4). For velocity-field backbones, the predictor-corrector mechanism also compares favorably with direct ODE integration: 200 NFEs of steps attain FID 4.91, compared with 6.51 for 800-step forward-Euler integration (Table 8).

To summarize, stationary probing offers an alternative to noise-to-data transport: any sample from the model target distribution already provides a valid initial state for the probability-preserving dynamics.

References

- [1] Yang Song, Jascha Sohl-Dickstein, Diederik P Kingma, Abhishek Kumar, Stefano Ermon, and Ben Poole. Score-based generative modeling through stochastic differential equations. In *International Conference on Learning Representations*, 2021. URL <https://openreview.net/forum?id=PXTIG12RRHS>.
- [2] Lars Ruthotto and Eldad Haber. An introduction to deep generative modeling. *GAMM-Mitteilungen*, 44(2):e202100008, 2021.
- [3] Georgios Batzolis, Jan Stanczuk, Carola-Bibiane Schönlieb, and Christian Etmann. Conditional image generation with score-based diffusion models. *arXiv preprint arXiv:2111.13606*, 2021.
- [4] Yang Song, Conor Durkan, Iain Murray, and Stefano Ermon. Maximum likelihood training of score-based diffusion models. *Advances in neural information processing systems*, 34: 1415–1428, 2021.
- [5] Yaron Lipman, Ricky TQ Chen, Heli Ben-Hamu, Maximilian Nickel, and Matt Le. Flow matching for generative modeling. *arXiv preprint arXiv:2210.02747*, 2022.
- [6] JL Lebowitz and E Rubin. Dynamical study of brownian motion. *Physical Review*, 131(6): 2381, 1963.
- [7] Ulrich G Haussmann and Etienne Pardoux. Time reversal of diffusions. *The Annals of Probability*, pages 1188–1205, 1986.
- [8] Yang Song and Stefano Ermon. Generative modeling by estimating gradients of the data distribution. In *Advances in Neural Information Processing Systems*, 2019.
- [9] Brian D. O. Anderson. Reverse-time diffusion equation models. *Stochastic Processes and their Applications*, 12(3):313–326, 1982.
- [10] Pascal Vincent. A connection between score matching and denoising autoencoders. *Neural Computation*, 23(7):1661–1674, 2011.
- [11] Prafulla Dhariwal and Alexander Nichol. Diffusion models beat gans on image synthesis. In *Advances in Neural Information Processing Systems*, volume 34, pages 8780–8794, 2021.
- [12] Patrick Lewis, Ethan Perez, Aleksandra Piktus, Fabio Petroni, Vladimir Karpukhin, Naman Goyal, Heinrich Küttler, Mike Lewis, Wen-tau Yih, Tim Rocktäschel, et al. Retrieval-augmented generation for knowledge-intensive nlp tasks. *Advances in neural information processing systems*, 33:9459–9474, 2020.
- [13] Robin Rombach, Andreas Blattmann, Dominik Lorenz, Patrick Esser, and Björn Ommer. High-resolution image synthesis with latent diffusion models. In *Proceedings of the IEEE/CVF Conference on Computer Vision and Pattern Recognition*, pages 10684–10695, 2022.
- [14] Andreas Blattmann, Robin Rombach, Kaan Oktay, Jonas Müller, and Björn Ommer. Retrieval-augmented diffusion models. In *Advances in Neural Information Processing Systems*, 2022.
- [15] Jonathan Ho, Ajay Jain, and Pieter Abbeel. Denoising diffusion probabilistic models. In *Advances in Neural Information Processing Systems*, volume 33, pages 6840–6851, 2020.
- [16] Giovanni Bussi and Michele Parrinello. Accurate sampling using langevin dynamics. *Physical Review E—Statistical, Nonlinear, and Soft Matter Physics*, 75(5):056707, 2007.
- [17] Gareth O. Roberts and Richard L. Tweedie. Exponential convergence of Langevin distributions and their discrete approximations. *Bernoulli*, 2(4):341–363, 1996.
- [18] Santosh Vempala and Andre Wibisono. Rapid convergence of the unadjusted langevin algorithm: Isoperimetry suffices. *Advances in neural information processing systems*, 32, 2019.
- [19] Yoshua Bengio, Aaron Courville, and Pascal Vincent. Representation learning: A review and new perspectives. *IEEE transactions on pattern analysis and machine intelligence*, 35(8): 1798–1828, 2013.

- [20] Yilun Du and Igor Mordatch. Implicit generation and modeling with energy based models. In *Advances in Neural Information Processing Systems*, 2019.
- [21] Katherine Keegan and Lars Ruthotto. Manifold-aware perturbations for constrained generative modeling. *arXiv preprint arXiv:2601.23151*, 2026.
- [22] Chen-Hao Chao, Wei-Fang Sun, Bo-Wun Cheng, and Chun-Yi Lee. On investigating the conservative property of score-based generative models. In *Proceedings of the 40th International Conference on Machine Learning*, volume 202 of *Proceedings of Machine Learning Research*, pages 4076–4095, 2023.
- [23] Anders Sjöberg, Jakob Lindqvist, Magnus Önnheim, Mats Jirstrand, and Lennart Svensson. MCMC-correction of score-based diffusion models for model composition. *arXiv preprint arXiv:2307.14012*, 2023.
- [24] Alain Durmus and Éric Moulines. Nonasymptotic convergence analysis for the unadjusted langevin algorithm. *The Annals of Applied Probability*, 27(3):1551–1587, 2017.
- [25] Gareth O. Roberts and Jeffrey S. Rosenthal. Optimal scaling of discrete approximations to Langevin diffusions. *Journal of the Royal Statistical Society: Series B*, 60(1):255–268, 1998.
- [26] Jerrold E. Marsden and Anthony J. Tromba. *Vector Calculus*. W. H. Freeman, 6 edition, 2011.
- [27] Kai Lai Chung. Markov chains. *Springer-Verlag, New York*, 1967.
- [28] Tianze Luo, Haotian Yuan, and Zhuang Liu. Soflow: Solution flow models for one-step generative modeling. *arXiv preprint arXiv:2512.15657*, 2025.
- [29] Sihyun Yu, Sangkyung Kwak, Huiwon Jang, Jongheon Jeong, Jonathan Huang, Jinwoo Shin, and Saining Xie. Representation alignment for generation: Training diffusion transformers is easier than you think. *arXiv preprint arXiv:2410.06940*, 2024.
- [30] Jia Deng, Wei Dong, Richard Socher, Li-Jia Li, Kai Li, and Li Fei-Fei. Imagenet: A large-scale hierarchical image database. In *2009 IEEE conference on computer vision and pattern recognition*, pages 248–255. Ieee, 2009.
- [31] Maria-Elena Nilsback and Andrew Zisserman. Automated flower classification over a large number of classes. In *Sixth Indian Conference on Computer Vision, Graphics & Image Processing*, pages 722–729. IEEE, 2008.
- [32] Aaron Van den Oord, Nal Kalchbrenner, Lasse Espeholt, Oriol Vinyals, Alex Graves, et al. Conditional image generation with pixelcnn decoders. *Advances in neural information processing systems*, 29, 2016.
- [33] Laurent Dinh, Jascha Sohl-Dickstein, and Samy Bengio. Density estimation using real nvp. *arXiv preprint arXiv:1605.08803*, 2016.
- [34] George Papamakarios, Eric Nalisnick, Danilo Jimenez Rezende, Shakir Mohamed, and Balaji Lakshminarayanan. Normalizing flows for probabilistic modeling and inference. *Journal of Machine Learning Research*, 22(57):1–64, 2021.
- [35] Diederik P Kingma and Max Welling. Auto-encoding variational bayes. *arXiv preprint arXiv:1312.6114*, 2013.
- [36] Danilo Jimenez Rezende, Shakir Mohamed, and Daan Wierstra. Stochastic backpropagation and approximate inference in deep generative models. In *International conference on machine learning*, pages 1278–1286. PMLR, 2014.
- [37] Ian J Goodfellow, Jean Pouget-Abadie, Mehdi Mirza, Bing Xu, David Warde-Farley, Sherjil Ozair, Aaron Courville, and Yoshua Bengio. Generative adversarial nets. *Advances in neural information processing systems*, 27, 2014.
- [38] Tero Karras, Samuli Laine, and Timo Aila. A style-based generator architecture for generative adversarial networks. In *Proceedings of the IEEE/CVF conference on computer vision and pattern recognition*, pages 4401–4410, 2019.

- [39] Jascha Sohl-Dickstein, Eric Weiss, Niru Maheswaranathan, and Surya Ganguli. Deep unsupervised learning using nonequilibrium thermodynamics. In *International conference on machine learning*, pages 2256–2265. pmlr, 2015.
- [40] Alexander Quinn Nichol and Prafulla Dhariwal. Improved denoising diffusion probabilistic models. In *International conference on machine learning*, pages 8162–8171. PMLR, 2021.
- [41] Ricky T. Q. Chen, Yulia Rubanova, Jesse Bettencourt, and David K. Duvenaud. Neural ordinary differential equations. In *Advances in Neural Information Processing Systems*, volume 31, 2018.
- [42] Will Grathwohl, Ricky TQ Chen, Jesse Bettencourt, Ilya Sutskever, and David Duvenaud. Ffjord: Free-form continuous dynamics for scalable reversible generative models. *arXiv preprint arXiv:1810.01367*, 2018.
- [43] Michael S Albergo and Eric Vanden-Eijnden. Building normalizing flows with stochastic interpolants. *arXiv preprint arXiv:2209.15571*, 2022.
- [44] Michael S. Albergo, Nicholas M. Boffi, and Eric Vanden-Eijnden. Stochastic interpolants: A unifying framework for flows and diffusions. *arXiv preprint arXiv:2303.08797*, 2023.
- [45] Xingchao Liu, Chengyue Gong, and Qiang Liu. Flow straight and fast: Learning to generate and transfer data with rectified flow. *arXiv preprint arXiv:2209.03003*, 2022.
- [46] Kirill Neklyudov, Rob Brekelmans, Daniel Severo, and Alireza Makhzani. Action matching: Learning stochastic dynamics from samples. In *International conference on machine learning*, pages 25858–25889. PMLR, 2023.
- [47] Bahjat Kawar, Michael Elad, Stefano Ermon, and Jiaming Song. Denoising diffusion restoration models. *Advances in neural information processing systems*, 35:23593–23606, 2022.
- [48] Yinhuai Wang, Jiwen Yu, and Jian Zhang. Zero-shot image restoration using denoising diffusion null-space model. *arXiv preprint arXiv:2212.00490*, 2022.
- [49] Chenlin Meng, Yutong He, Yang Song, Jiaming Song, Jiajun Wu, Jun-Yan Zhu, and Stefano Ermon. Sdedit: Guided image synthesis and editing with stochastic differential equations. *arXiv preprint arXiv:2108.01073*, 2021.
- [50] Jiaming Song, Chenlin Meng, and Stefano Ermon. Denoising diffusion implicit models. *arXiv preprint arXiv:2010.02502*, 2020.
- [51] Amir Hertz, Ron Mokady, Jay Tenenbaum, Kfir Aberman, Yael Pritch, and Daniel Cohen-Or. Prompt-to-prompt image editing with cross attention control. *arXiv preprint arXiv:2208.01626*, 2022.
- [52] Ron Mokady, Amir Hertz, Kfir Aberman, Yael Pritch, and Daniel Cohen-Or. Null-text inversion for editing real images using guided diffusion models. In *Proceedings of the IEEE/CVF conference on computer vision and pattern recognition*, pages 6038–6047, 2023.
- [53] Olaf Ronneberger, Philipp Fischer, and Thomas Brox. U-net: Convolutional networks for biomedical image segmentation. In *International Conference on Medical image computing and computer-assisted intervention*, pages 234–241. Springer, 2015.
- [54] John Charles Butcher. *Numerical methods for ordinary differential equations*. John Wiley & Sons, 2016.
- [55] William Peebles and Saining Xie. Scalable diffusion models with transformers. In *Proceedings of the IEEE/CVF international conference on computer vision*, pages 4195–4205, 2023.

Appendix Outline

The appendices are organized as follows:

- Appendix A discusses related work relevant to our methods.
- Appendix B derives the denoiser used at sampling time from a pretrained flow-matching model, with a general formula for any linear bridge $x_t = \kappa(t)x + \sigma(t)z$ and an explicit specialization to the linear interpolant $x_t = tx + (1 - t)z$.
- Appendix C provides explicit pseudocode for one step of the Denoiser-Metropolis (dMALA) sampler (Algorithm 1) and the Predictor–Corrector sampler (Algorithm 2), together with the cancellation argument that takes the trapezoidal line-integral acceptance ratio of Section 2.2 into the simple two-evaluation form used in our experiments.
- Appendix D describes the datasets, pretrained backbones (SoFlow-XL/2-cond and SiT-REPA-XL), the Flowers-102 U-Net architecture, and the compute used.
- Appendix E reports additional quantitative results: an evaluation on Oxford Flowers-102 and a dMALA ablation over smoothing levels σ and chain lengths K on ImageNet-256 with the SoFlow backbone, in addition to a study on the computational efficiency of our method.
- Appendix F discusses broader societal impact.
- Appendix G shows generated-sample visualizations across step counts on Flowers-102 and ImageNet-256.

A Related Work

Generative Modeling. Deep generative models have progressed from autoregressive networks [32], exact-likelihood normalizing flows [33, 34], and variational autoencoders [35, 36] to generative adversarial networks capable of high-resolution synthesis [37, 38]. More recently, denoising diffusion probabilistic models [39, 15, 40] have achieved state-of-the-art sample quality by learning to reverse a gradual noising process. While these foundational models predominantly focus on mapping a simple noise prior to the target data distribution, our work provides a complementary framework that operates directly within the data distribution itself.

Continuous-Time Transport and Flows. The generative processes of diffusion can be elegantly unified through the lens of continuous-time differential equations [41, 42]. Recent formulations such as stochastic interpolants [43, 44], rectified flows [45], and action matching [46] learn ordinary differential equations (ODEs) to smoothly transport probability mass from a base distribution to the target data. While traditionally optimized for efficient, straight-path generation from pure noise, the vector fields learned by these models provide the fundamental continuous-time dynamics that our predictor-corrector mechanism repurposes for local probability-preserving exploration.

Data-Supported Initialization. Beyond unconditional generation from noise, initializing stochastic processes from data-supported states is widely used in inverse problems [47, 48] and guided image editing. Methods like SDEdit [49] inject controlled noise into an existing sample and reverse the process to produce realistic modifications, while deterministic inversion techniques map real data into latent spaces for localized semantic editing [50, 51, 52]. Although these methods primarily aim to balance user-guided constraints with sample realism, they share the underlying principle of exploring the local geometry around a given data manifold—a property we explicitly formalize as a stationary generative kernel.

B Estimating a Denoiser from a Flow Model

A practical advantage of our framework is that it can reuse pretrained flow-matching models. In many settings, strong flow models are already available, and it is desirable to use them directly rather than train a separate denoiser. The key point is that the bridge used in flow matching already defines a consistent denoising problem near the data manifold. Thus a pretrained flow model can be converted into a denoiser in a way that is fully consistent with the interpolation on which it was trained.

Consider a general linear bridge

$$x_t = \kappa(t)x + \sigma(t)z, \quad x \sim p, \quad z \sim \mathcal{N}(0, I), \quad (32)$$

where $t \in [0, 1]$, $\kappa(1) = 1$, and $\sigma(1) = 0$. To connect this bridge to denoising, define a noisy variable

$$x_\eta = x + \eta z. \quad (33)$$

If we choose

$$\eta = \frac{\sigma(t)}{\kappa(t)}, \quad (34)$$

then

$$\kappa(t)x_\eta = \kappa(t)x + \kappa(t)\eta z = \kappa(t)x + \sigma(t)z = x_t. \quad (35)$$

Thus the bridge variable x_t is simply a scaled version of the noisy sample x_η .

Suppose first that the pretrained flow model provides a direct solution map

$$f_\theta(x_t, t, 1) \approx x, \quad (36)$$

that maps a point at time t to its prediction at time 1. Then, using Equation (35), the denoiser associated with noise level η is

$$D_\eta(y) := \mathbb{E}[x | x_\eta = y] \approx f_\theta(\kappa(t)y, t, 1), \quad \eta = \frac{\sigma(t)}{\kappa(t)}. \quad (37)$$

This is the simplest and most useful form in practice: one evaluates the flow model at the scaled point $\kappa(t)y$, not at y itself.

If instead the pretrained model provides only a velocity field

$$v_\theta(x_t, t) \approx \mathbb{E}[\dot{x}_t | x_t], \quad (38)$$

then the denoiser can still be recovered. Differentiating Equation (32) gives

$$\dot{x}_t = \kappa'(t)x + \sigma'(t)z. \quad (39)$$

Together, Equation (32) and Equation (39) form a 2×2 linear system in x and z . Solving for x gives

$$x = \frac{\sigma'(t)x_t - \sigma(t)\dot{x}_t}{\kappa(t)\sigma'(t) - \kappa'(t)\sigma(t)}. \quad (40)$$

Substituting $x_t = \kappa(t)y$ with $y = x_\eta$ and taking conditional expectations yields

$$D_\eta(y) \approx \frac{\sigma'(t)\kappa(t)y - \sigma(t)v_\theta(\kappa(t)y, t)}{\kappa(t)\sigma'(t) - \kappa'(t)\sigma(t)}, \quad \eta = \frac{\sigma(t)}{\kappa(t)}. \quad (41)$$

Again, the input to the flow model is the scaled point $\kappa(t)y$.

For the linear bridge used in our experiments,

$$x_t = tx + (1-t)z, \quad (42)$$

we have $\kappa(t) = t$, $\sigma(t) = 1 - t$, and therefore

$$\eta = \frac{1-t}{t}. \quad (43)$$

In this case the denoiser induced by a direct solution map is simply

$$D_\eta(y) \approx f_\theta(ty, t, 1), \quad t = \frac{1}{1+\eta}. \quad (44)$$

If one uses the velocity field instead, then Equation (41) reduces to

$$D_\eta(y) \approx ty + (1-t)v_\theta(ty, t), \quad t = \frac{1}{1+\eta}. \quad (45)$$

This construction is important for two reasons. First, it lets us use strong pretrained flow-matching codes directly as denoisers near the data manifold. Second, it keeps the method internally consistent: the same bridge used in training defines the denoiser used at sampling time. In particular, if t is chosen close to 1, then η is small, the denoiser acts only in a narrow neighborhood of the data manifold, and the resulting corrected sampler operates in exactly the regime on which the flow model was trained.

C Algorithmic Details

This appendix gives explicit pseudocode for one step of each of the two probability-preserving samplers introduced in Section 2, and the short cancellation argument that turns the line-integral acceptance ratio of Section 2.2 into the simple two-evaluation form actually used in our experiments.

C.1 Denoiser-Metropolis (dMALA) Sampler

dMALA combines the proposal Equation (16) with the simplified acceptance ratio Equation (21). One step requires exactly two evaluations of the denoiser: one at the current state and one at the proposed state (Algorithm 1).

Algorithm 1 One step of the Denoiser-Metropolis (dMALA) sampler.

Require: current state x_j , denoiser D_σ , smoothing level $\sigma > 0$

- 1: Draw $z \sim \mathcal{N}(0, I)$.
- 2: Form the proposal $y = D_\sigma(x_j) + \sqrt{2}\sigma z$. (cf. Equation (16))
- 3: Compute the approximate log-acceptance ratio

$$\log r_{D_\sigma}(x_j, y) \approx \frac{1}{4\sigma^2} \left(\|D_\sigma(x_j) - x_j\|^2 - \|D_\sigma(y) - y\|^2 \right).$$

(cf. Equation (21))

- 4: Set $\alpha = \min\{1, \exp(\log r_{D_\sigma}(x_j, y))\}$.
- 5: Draw $u \sim \text{Unif}(0, 1)$.
- 6: **if** $u \leq \alpha$ **then**
- 7: Set $x_{j+1} = y$. {accept}
- 8: **else**
- 9: Set $x_{j+1} = x_j$. {reject}
- 10: **end if**

Ensure: x_{j+1}

C.2 Predictor–Corrector Sampler

The predictor–corrector sampler combines a single Gaussian noising step at the bridge time τ with the application of the learned flow map $\Phi_{\theta, \tau \rightarrow 1}$ back to the data end of the bridge (Algorithm 2). Any procedure that realizes this flow map suffices, and our framework is agnostic to the choice. When the pretrained model exposes a direct solution map $f_\theta(\cdot, \tau, 1)$ as for SoFlow [28], the corrector is a single network function evaluation (NFE). When the model is given as a velocity field v_θ as for SiT-REPA-XL [29], the flow map is realized by numerically integrating $\dot{x} = v_\theta(x, t)$ from $t = \tau$ to $t = 1$ using any ODE integrator of choice; in our experiments we use forward Euler with n_{steps} steps (Table 8), but Runge–Kutta variants, DPM-Solver, or any other integrator would equally well realize the same flow map. The total cost per probe iteration is therefore 1 NFE for a direct solution map and n_{steps} NFEs for a numerically integrated velocity field.

Algorithm 2 One step of the Predictor–Corrector sampler.

Require: current state x_j , bridge time $\tau \in (0, 1)$, flow map $\Phi_{\theta, \tau \rightarrow 1}$

- 1: **Predictor:** draw $z \sim \mathcal{N}(0, I)$ and set $\hat{x} \leftarrow (1 - \tau)z + \tau x_j$. Equation (28)
- 2: **Corrector:** set $x_{j+1} \leftarrow \Phi_{\theta, \tau \rightarrow 1}(\hat{x})$.

Ensure: x_{j+1}

C.3 Derivation of the Trapezoidal Acceptance Ratio

We give the cancellation argument that takes the trapezoidal approximation of the line integral in Equation (20) into the simple two-evaluation form used in Equation (21).

Recall that the corrected log-acceptance ratio is

$$\log r_{D_\sigma}(x, y) = \Delta_{D_\sigma}(x, y) + \log q_\sigma(x | y) - \log q_\sigma(y | x), \quad (46)$$

with proposal density $q_\sigma(y | x) = \mathcal{N}(y; D_\sigma(x), 2\sigma^2 I)$. The Gaussian proposal log-ratio is

$$\log q_\sigma(x | y) - \log q_\sigma(y | x) = \frac{1}{4\sigma^2} \left(\|y - D_\sigma(x)\|^2 - \|x - D_\sigma(y)\|^2 \right). \quad (47)$$

Writing $r_\sigma(x) := D_\sigma(x) - x$, expand each squared norm:

$$\|y - D_\sigma(x)\|^2 = \|(y - x) - r_\sigma(x)\|^2 = \|y - x\|^2 - 2 \langle y - x, r_\sigma(x) \rangle + \|r_\sigma(x)\|^2, \quad (48)$$

$$\|x - D_\sigma(y)\|^2 = \|(x - y) - r_\sigma(y)\|^2 = \|y - x\|^2 - 2 \langle x - y, r_\sigma(y) \rangle + \|r_\sigma(y)\|^2. \quad (49)$$

Subtracting and using $\langle x - y, r_\sigma(y) \rangle = -\langle y - x, r_\sigma(y) \rangle$,

$$\|y - D_\sigma(x)\|^2 - \|x - D_\sigma(y)\|^2 = -2 \langle y - x, r_\sigma(x) + r_\sigma(y) \rangle + \|r_\sigma(x)\|^2 - \|r_\sigma(y)\|^2. \quad (50)$$

Substituting Equation (50) into Equation (47) and combining with the trapezoidal approximation $\Delta_{D_\sigma}(x, y) \approx \frac{1}{2\sigma^2} \langle r_\sigma(x) + r_\sigma(y), y - x \rangle$, the inner-product terms cancel and only the squared-residual difference survives:

$$\log r_{D_\sigma}(x, y) \approx \frac{1}{4\sigma^2} \left(\|D_\sigma(x) - x\|^2 - \|D_\sigma(y) - y\|^2 \right), \quad (51)$$

which is Equation (21). The sampler therefore needs only two evaluations of D_σ per step, one at the current state and one at the proposal.

D Experimental Details

D.1 Datasets

Oxford Flowers-102. We use the Oxford 102 Category Flower dataset [31], which comprises 8,189 images spanning 102 fine-grained flower species. All three official splits (train, validation, and test) are merged into a single evaluation pool, following prior unconditional generation work. All images are resized to 256×256 pixels.

ImageNet-256. For large-scale experiments we use ImageNet 2012 [30] at 256×256 resolution with 1,000 classes. Generation operates in the latent space of a variational autoencoder [13], following the convention of recent latent generative models such as REPA [29].

D.2 Generative Models

All three backbones share the same variational autoencoder [13], a KL-regularized encoder–decoder trained to produce 4-channel latents at $1/8$ the spatial resolution of the input image (i.e. 32×32 for 256×256 inputs). Latents are scaled by $\lambda = 0.18215$ before and after the generative model, following the convention of the Stable Diffusion codebase.

D.2.1 Oxford Flowers-102

For the Flowers-102 experiments we train a latent flow matching model from scratch using a U-Net [53] that operates directly on the 4-channel latent tensors. The architecture is summarized in Table 5. The model is trained with a cosine-path interpolant

$$x_t = \cos\left(\frac{\pi}{2}t\right) x + \sin\left(\frac{\pi}{2}t\right) \varepsilon, \quad x \sim p, \varepsilon \sim \mathcal{N}(0, I), \quad (52)$$

so that $t = 0$ corresponds to pure data and $t = 1$ to pure noise. Generation from noise integrates the learned velocity backward from $t = 1$ to $t = 0$ using the second-order Runge–Kutta (RK2) integrator [54].

D.2.2 ImageNet-256

SoFlow [28] is a class-conditional latent flow matching model built on the DiT-XL/2 backbone [55]. We use the publicly available checkpoint trained for 1.2×10^6 gradient steps with the EMA model weights. The model uses a linear interpolant

$$x_t = (1 - t) z + t x, \quad t \in [0, 1], \quad (53)$$

Table 5: Flow Matching U-Net architecture (Flowers-102).

Hyperparameter	Value
Latent channels	4
Latent resolution	32×32
Residual blocks per level	3
Channel multipliers	[1, 2, 2, 2]
Attention heads	4
Attention resolutions	16×16
Dropout	0.1
Interpolant	Cosine path
ODE integrator	RK2, $N_{\text{ode}} = 10$

with the Euler coefficient type, operating on 32×32 4-channel latents and conditioning on 1,000 ImageNet class labels.

We additionally use the SiT-XL/2 checkpoint trained with REPA [29], a training objective that aligns a DiT’s internal representations with a frozen vision encoder. We generate 50,000 samples and evaluate using the REPA evaluator script. For both backbones, all generations reported in this paper are produced without classifier-free guidance.

D.3 Implementation Details

All experiments for Oxford Flowers-102 ran on a single NVIDIA RTX 4090 GPU. ImageNet-256 experiments used two NVIDIA RTX 4090 GPUs and one H100 GPU. We did not retrain or finetune any of the pretrained ImageNet backbones (SoFlow-XL/2-cond, SiT-REPA-XL); the 50,000-sample evaluation runs are the only ImageNet-scale compute consumed by our framework.

E Additional Experimental Results

E.1 Oxford Flowers-102

We evaluate our approach on the Oxford Flower-102 dataset [31] (training details are in D.2.1). Table 6 compares the Predictor–Corrector and dMALA samplers against a standard flow-matching baseline generated from Gaussian noise, reporting Frechet Inception Distance (FID), Precision, and Recall across step counts.

Table 6: FID, Precision, and Recall on Oxford Flowers-102, with $t_{\text{noise}} = 0.1$.

Method	Steps	FID ↓	Precision ↑	Recall ↑
Baseline FM (noise → data)	–	23.95	0.5213	0.2761
Predictor–Corrector	20	12.50	0.6013	0.6962
	40	15.90	0.4676	0.6313
	60	19.92	0.3859	0.5848
	80	25.38	0.3091	0.5524
dMALA	20	10.92	0.6967	0.7825
	40	12.64	0.5940	0.6936
	60	14.45	0.5179	0.6537
	80	16.34	0.4587	0.6210

E.2 ImageNet-256: dMALA Ablation

Table 7 reports the dMALA sampler on ImageNet-256 with the SoFlow-XL/2-cond backbone, sweeping the smoothing level σ at $\sigma \in \{0.3, 0.5\}$ and the number of Metropolis–Hastings iterations K . Smaller σ raises the acceptance rate and yields lower FID; larger σ trades FID against higher Inception Score and Precision, at the cost of Recall.

Table 7: dMALA on ImageNet-256 with SoFlow-XL/2-cond. The denoiser uses SoFlow’s solution operator with noise level σ . K denotes the number of Metropolis–Hastings iterations; Acc. rate is the running mean acceptance probability. Metrics are computed on 50,000 samples against the ADM reference batch. Reference baseline shown in gray.

	K	Acc. rate	FID ↓	sFID ↓	IS ↑	Precision ↑	Recall ↑
Baseline (1-NFE)	–	–	2.96	4.60	238.53	0.80	0.56
$\sigma = 0.5$	50	0.68	5.50	6.57	356.05	0.87	0.47
	100	0.49	7.28	8.18	367.45	0.89	0.42
	150	0.49	8.29	9.49	372.80	0.89	0.39
	200	0.48	9.02	10.32	377.30	0.90	0.38
$\sigma = 0.3$	50	0.76	3.23	7.72	313.29	0.81	0.57
	100	0.54	4.34	10.40	308.11	0.82	0.52
	150	0.53	5.07	12.45	301.23	0.81	0.49
	200	0.53	5.61	14.26	294.47	0.81	0.47

E.3 Computational Efficiency

In the next experiment we test the computational efficiency of the methods and compare them for a transport generation that has a similar budget. Results are shown in Table 8.

Table 8: Predictor–corrector sampling matches or beats direct flow integration at equal or smaller compute on ImageNet-256 with SiT-REPA-XL. The baseline rows integrate the learned velocity field v_θ from $t=1$ to $t=0$ using forward Euler with the indicated number of steps. Our method runs the Algorithm 2 sampler for K predictor–corrector iterations; the corrector inside each iteration integrates v_θ from $t=\tau$ to $t=1$ using forward Euler with n_{steps} steps, so the total network function evaluations satisfy $\text{NFE} = n_{\text{steps}} \cdot K$. All our methods use $t_{\text{noise}}=0.5$. Metrics are computed on 50,000 samples against the ADM reference batch.

	NFE	FID ↓	sFID ↓	IS ↑	Precision ↑	Recall ↑
Baseline (400 Euler steps)	400	6.61	5.62	152.52	0.68	0.69
Baseline (800 Euler steps)	800	6.51	5.58	153.08	0.68	0.69
Pred.–Corr $n_{\text{steps}}=10, K=20$ (ours)	200	4.91	12.07	183.82	0.70	0.66
Pred.–Corr $n_{\text{steps}}=20, K=20$ (ours)	400	3.06	6.24	199.50	0.72	0.69

F Broader Impact

This work develops a sampling framework that operates on top of existing pretrained flow-matching models. Two implications follow. On the positive side, because our framework re-uses existing checkpoints rather than training new generative models, it can reduce the energy and compute footprint of deploying generative systems, and pairs naturally with retrieval-augmented pipelines that aim to ground generated content in reliable source material. On the negative side, because the framework inherits the behavior of the underlying pretrained model, it also inherits whatever biases, representational gaps, or potential for misuse the underlying model carries, including the risk of being applied to produce deepfakes or targeted misinformation. Practitioners deploying this framework should treat the underlying model’s documentation and known failure modes as a baseline that the sampling framework does not modify.

G Sample Visualizations

We provide visualizations of both the Predictor–Corrector and the dMALA samplers on the ImageNet256 dataset [30]. Figure 5 presents a combined high-resolution overview comparing both methods across the SoFlow-XL/2 and SiT-XL/2 models over 200 iterations.

To examine the short-term behavior of the samplers, Figure 6 and Figure 7 illustrate the original images alongside samples generated after a 20-step run using dMALA and Predictor–Corrector, respectively.

Furthermore, we provide extended long-run visualizations for Predictor–Corrector in Figure 8 and for dMALA in Figure 9. In these extended subfigures, the first row displays the original image (before any iterations), and each subsequent row corresponds to an additional 50 steps, reaching 200 steps in the final row. Across all experiments, both methods successfully preserve the class identity throughout the chain while progressively moving the sample along the data manifold. To further illustrate the step-by-step progression of the Predictor–Corrector across longer chains, Figure 10 and Figure 11 present generated samples using the SiT-REPA-XL and SoFlow-XL/2-cond backbones, respectively. In these figures, the leftmost column presents the original image, while the subsequent columns track the continuous evolution of the state across steps.

G.1 ImageNet-256

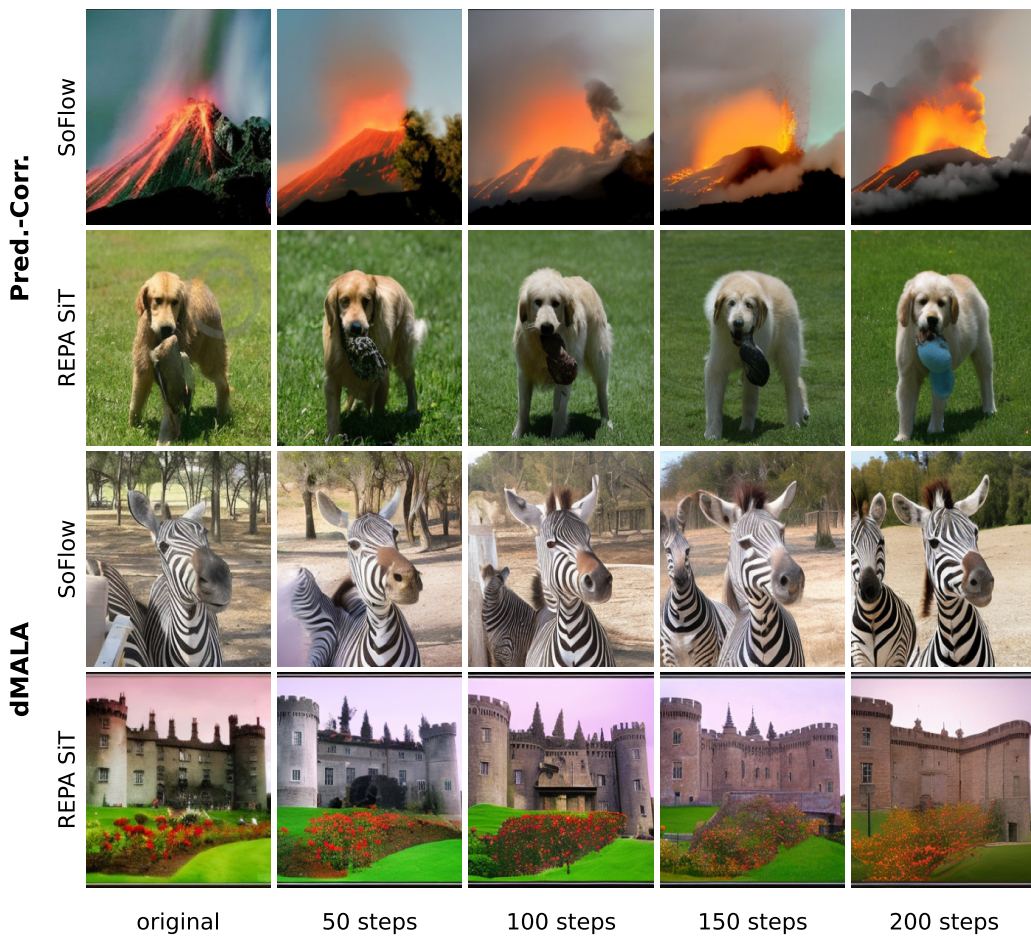


Figure 5: Visualization of ImageNet256 for two methods (Predictor–Corrector and dMALA) and two models (SoFlow-XL/2 and REPA SiT-XL/2). The first column shows the original image; each subsequent column shows the sample after an additional 50 iterations, up to 200 total.

G.2 Oxford Flowers-102 Visualization

We further validate our approach on the Oxford Flowers dataset [31]. Figure 12 shows results for the Predictor–Corrector and dMALA. In each subfigure the first row shows the original image, and each subsequent row shows the sample after an additional 20 iterations.



(a) SoFlow-XL/2

(b) SiT-XL/2

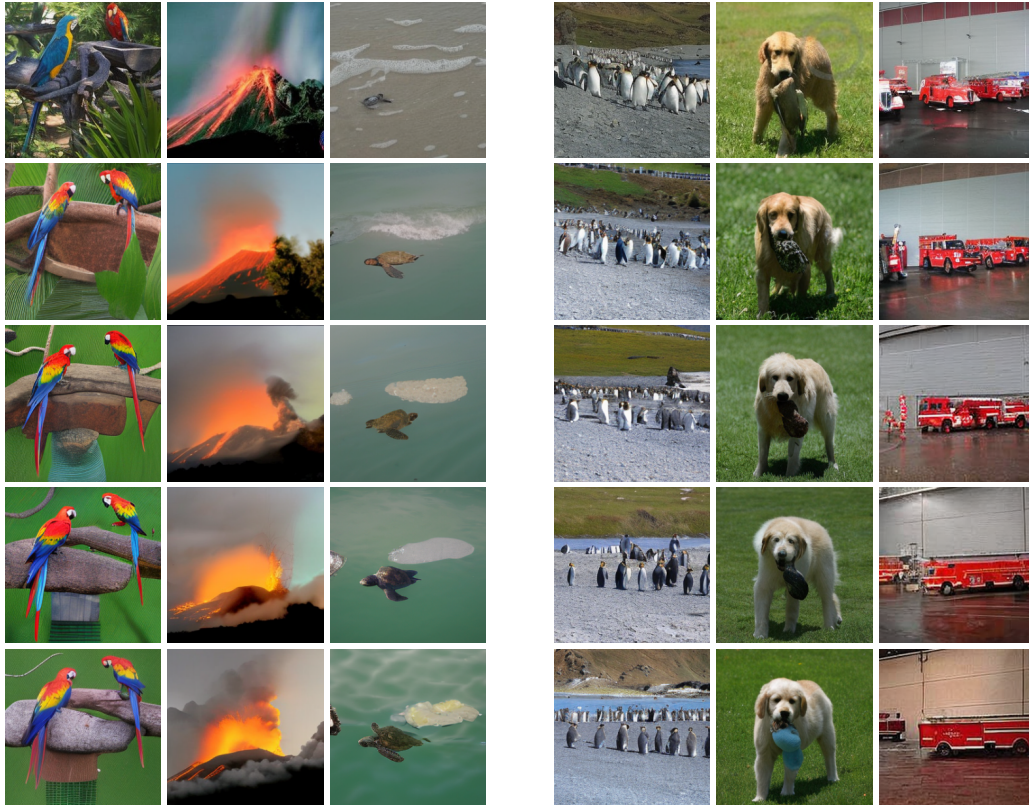
Figure 6: dMALA (20 steps). The first row shows the original image; the second row shows the generated sample.



(a) SoFlow-XL/2

(b) SiT-XL/2

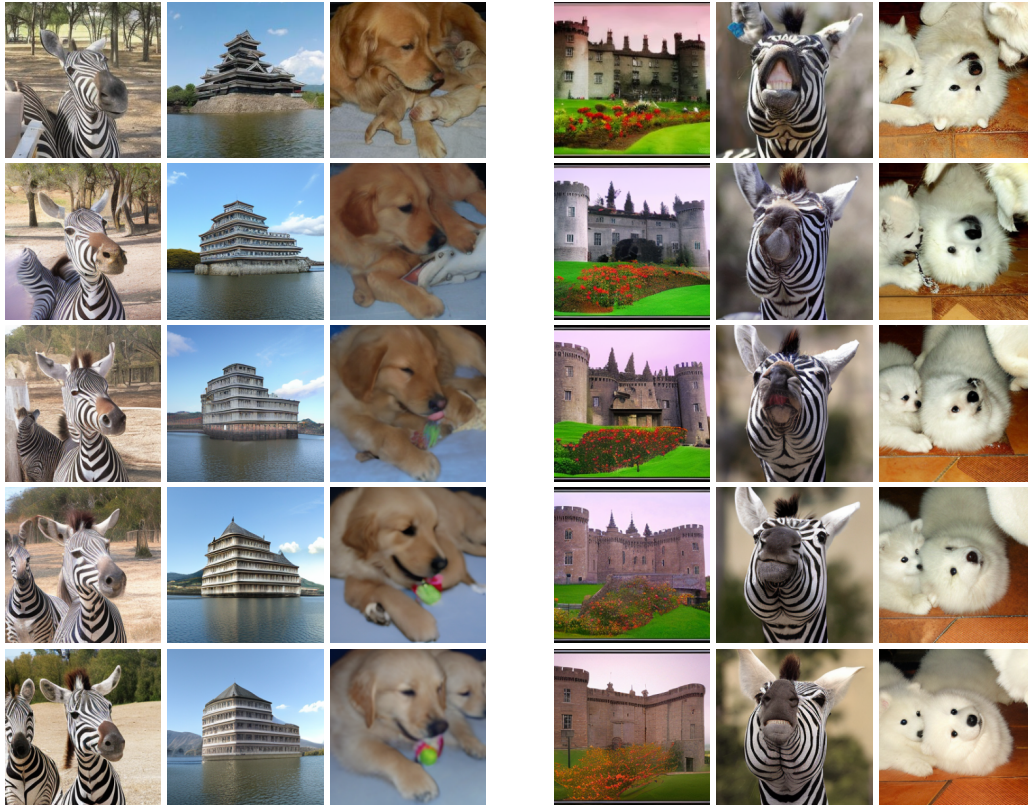
Figure 7: Pred.-Corr. (20 steps). The first row shows the original image; the second row shows the generated sample.



(a) SoFlow-XL/2

(b) SiT-XL/2

Figure 8: Predictor–Corrector on ImageNet256 over 200 iterations. The first row shows the original image; each subsequent row shows the sample after an additional 50 steps, up to a total of 200 steps.



(a) SoFlow-XL/2

(b) SiT-XL/2

Figure 9: dMALA on ImageNet256 over 200 iterations. The first row shows the original image; each subsequent row shows the sample after an additional 50 steps, up to a total of 200 steps.

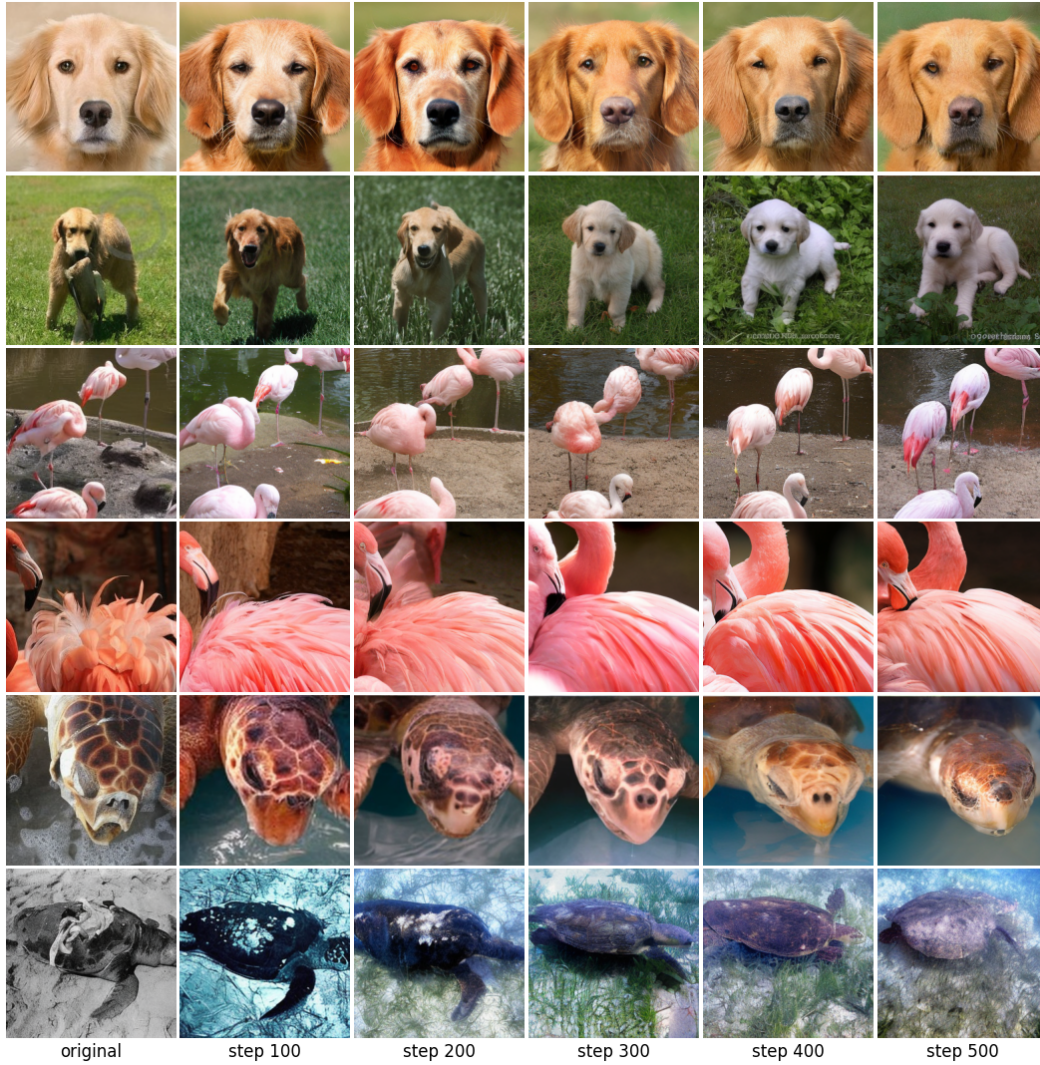


Figure 10: Pred.-Corr. ImageNet-256 samples generated by with the SiT-REPA-XL backbone. The leftmost column shows the original image; subsequent columns show the state after the indicated number of probe iterations.

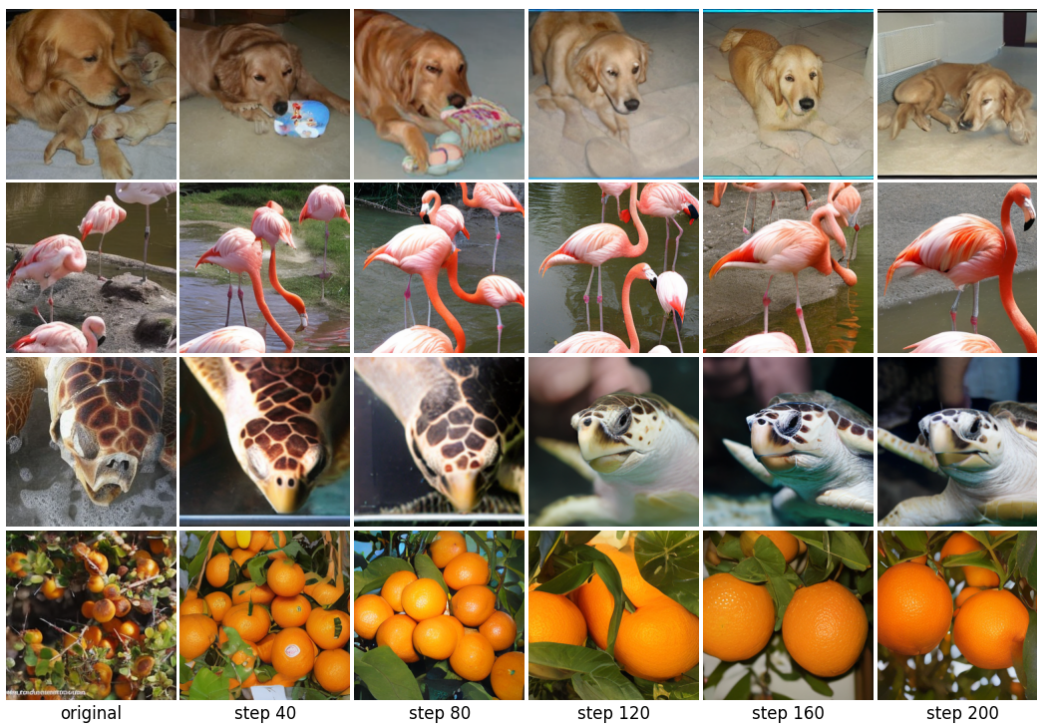
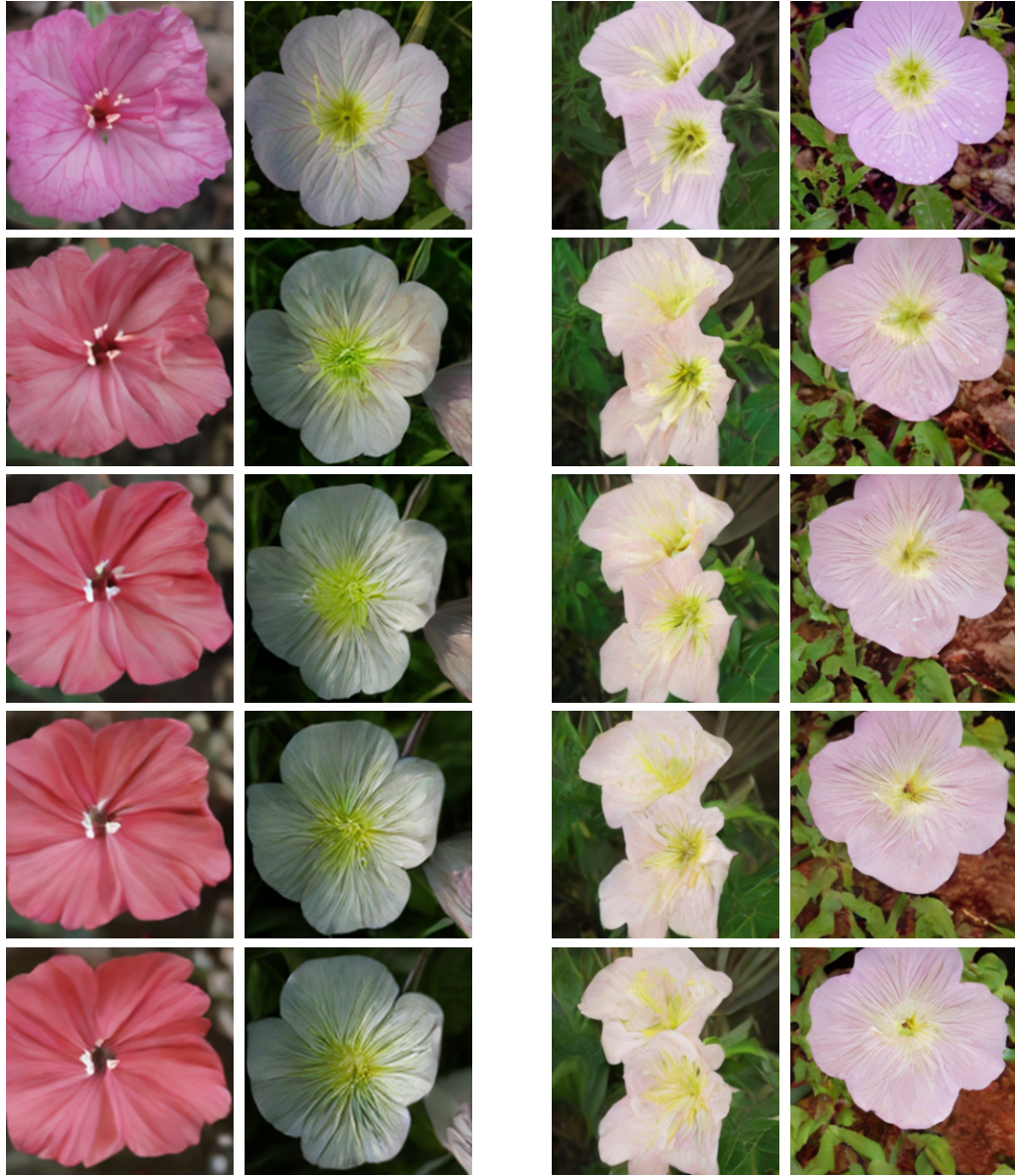


Figure 11: Pred.-Corr. ImageNet-256 samples generated by with the SoFlow-XL/2-cond backbone. The leftmost column shows the original image; subsequent columns show the state after the indicated number of probe iterations.



(a) Predictor–Corrector

(b) dMALA

Figure 12: Predictor–Corrector and dMALA on Oxford Flowers-102 over 80 iterations. The first row shows the original image; each subsequent row shows the sample after an additional 20 iterations, up to a total of 80 steps.